nature communications

Article

https://doi.org/10.1038/s41467-024-51896-4

Optically selective catalyst design with minimized thermal emission for facilitating photothermal catalysis

Received: 24 April 2024

Accepted: 19 August 2024

Published online: 01 September 2024

Check for updates

Zhengwei Yang[1,8], Zhen-Yu Wu[2,3,8], Zhexing Lin[1,8], Tianji Liu[4], Liping Ding[5,6], Wenbo Zhai[7], Zipeng Chen[1], Yi Jiang[1], Jinlei Li[1], Siyun Ren[1], Zhenhui Lin[1], Wangxi Liu[1], Jianyong Feng[1], Xing Zhang[1], Wei Li[4], Yi Yu[7], Bin Zhu[1] ✉, Feng Ding[6], Zhaosheng Li[1] & Jia Zhu[1] ✉

Converting solar energy into fuels is pursued as an attractive route to reduce dependence on fossil fuel. In this context, photothermal catalysis is a very promising approach through converting photons into heat to drive catalytic reactions. There are mainly three key factors that govern the photothermal catalysis performance: maximized solar absorption, minimized thermal emission and excellent catalytic property of catalyst. However, the previous research has focused on improving solar absorption and catalytic performance of catalyst, largely neglected the optimization of thermal emission. Here, we demonstrate an optically selective catalyst based $Ti_3C_2T_x$ Janus design, that enables minimized thermal emission, maximized solar absorption and good catalytic activity simultaneously, thereby achieving excellent photothermal catalytic performance. When applied to Sabatier reaction and reverse water-gas shift (RWGS) as demonstrations, we obtain an approximately 300% increase in catalytic yield through reducing the thermal emission of catalyst by ~70% under the same irradiation intensity. It is worth noting that the CO_2 methanation yield reaches 3317.2 mmol g_{Ru}^{-1} h^{-1} at light power of 2 W cm^{-2}, setting a performance record among catalysts without active supports. We expect that this design opens up a new pathway for the development of high-performance photothermal catalysts.

Efficient utilization of solar energy[1] to produce highly value-added fuels and chemicals is being pursued to reduce dependence on fossil fuel[2–7]. Particularly, photothermal catalysis, converting clean photons into heat to drive catalytic processes via various mechanisms[8–12], has attracted wide attention. To boost the solar-to-chemical energy conversion efficiency via photothermal effect[13,14], it is critical to generate the required temperature with lower light power and to facilitate the catalytic process thermodynamically and kinetically over a long period of time[15–17].

For maximizing the photothermal conversion, it is important to consider the net heating power of the catalyst from a heat balance analysis:

$$\begin{aligned} P_{heat} &= P_{light} - P_{rad} - P_{conduction-convection} \\ &= P_{sun} - \varepsilon\sigma T^4 - P_{conduction-convection} \\ &= \int I_{light}(\lambda)\alpha(\lambda)d\lambda - \int I_{BB}(T,\lambda)\varepsilon(\lambda)d\lambda - h(T_{surface} - T_{ambient}) \end{aligned} \quad (1)$$

Where ε is average emissivity, σ is Stefan–Boltzmann constant, $I_{light}(\lambda)$ is the energy distribution under the solar illumination of the AM1.5 spectrum, $I_{BB}(T, \lambda)$ is the energy distribution under the radiation

A full list of affiliations appears at the end of the paper. ✉e-mail: binzhu@nju.edu.cn; jiazhu@nju.edu.cn

spectrum of a blackbody at a given temperature T, $\alpha(\lambda)$ is absorptance at a given wavelength, $\varepsilon(\lambda)$ is emissivity at a given wavelength and $P_{conduction-convection}$ is the power caused by conduction and convection.

It is clear that to maximize the photothermal conversion, the ideal design is to enable maximized sunlight absorption (α_{light}) (0.28–2.5 μm) and minimized thermal emission (mid-infrared emissivity, ε_{MIR}) simultaneously, especially under high-intensity solar irradiation (Fig. 1a, b, Supplementary Fig. 1, Supplementary Tables 1–3 and Supplementary Note 1)[18,19]. For example, for a temperature of ~620 K, a common temperature for chemical reactions, the thermal emission from catalysts (under a light input power of 2 W cm^{-2}) results in an energy loss of ~0.83 W cm^{-2} (accounts for 41.5% of the input light power), thereby significantly decreasing the energy conversion efficiency (Supplementary Note 2). For the part of enhancing the catalytic activity and stability, the ideal design is to facilitate the mass transfer of reactants and products[2], while preventing catalysts from sintering and coking, especially at high temperature[20,21].

Recent years have witnessed significant efforts and advancements in the field of photothermal catalysis. Notably, Ouyang et al. demonstrated the significant enhancement of α_{light} by employing novel defect engineering on In_2O_3, leading to improved performance in photothermal catalysis[22]. He et al. proposed an elegant greenhouse design to confine the photothermal energy[23]. Ozin and He proposed Nb_2C and Mo_2TiC_2-based catalysts for optimizing full spectrum absorption[24,25]. Ye et al. innovatively integrated catalysts and spectral selective external reactors, to effectively facilitate photothermal catalysis[26,27]. While several MXene structures demonstrate promising thermal emission properties[28–33], and the MXene-based catalysts have been efficiently utilized in catalytic reactions[24,25], the ideal photothermal catalysts, which possess three properties simultaneously: high solar absorption, low thermal emission, and activated catalytic process, remain unrealized thus far.

Herein, we propose and demonstrate an optically selective catalyst with $Ti_3C_2T_x$-based Janus design composed of overlying flat $Ti_3C_2T_x$ flake layers and underlying hollow $Ti_3C_2T_x$ spheres, which minimizes thermal emission, maximizes solar absorption and good catalytic activity simultaneously, thus achieving excellent photothermal catalytic performance (Fig. 1c). Specifically, the high in-plane permittivity (mid-infrared) of overlying flat $Ti_3C_2T_x$ flake layers enables high α_{light} (~88%) and low ε_{MIR} (~21%), ideal for the photothermal effect (Fig. 1d)[28–33]; while the underlying hollow $Ti_3C_2T_x$ spheres can facilitate the mass transfer of reactants and products, beneficial for the catalytic activity. Furthermore, this universal architecture can be integrated with various metal nanoparticle catalysts (e.g., ruthenium, palladium, nickel) for a wide range of reactions. When employed in the Sabatier reaction and reverse water-gas shift (RWGS), we demonstrated that reducing the ε_{MIR} by ~70% can lead to an approximately 300% increase in catalytic yield. Among them, the CO_2 methanation yield reaches 3317.2 mmol g_{Ru}^{-1} h^{-1} at a light power of 2 W cm^{-2}, setting a performance record among catalysts without active supports.

Results

Synthesis and characterization of the designed photothermal host and Ru-loaded MXene catalyst (Ru@m-$Ti_3C_2T_x$)

To simultaneously achieve high solar absorption, low thermal emission, and activated catalytic process in the catalyst, we employed a two-step approach including a hard-templated method and subsequent impregnation, constructing the photothermal host with selective spectrum and porous structure (Fig. 2a–e, details seen in Methods)[34–36]. To create the ideal photothermal layer, we utilized negative pressure during suction filtration to create the flat $Ti_3C_2T_x$ flake layers (Fig. 2e). Noted that the intrinsic selective spectrum of $Ti_3C_2T_x$ is dependent on its structure (details seen in Fig. 3 below). As the presence of channels for advancing mass transfer of reactants and

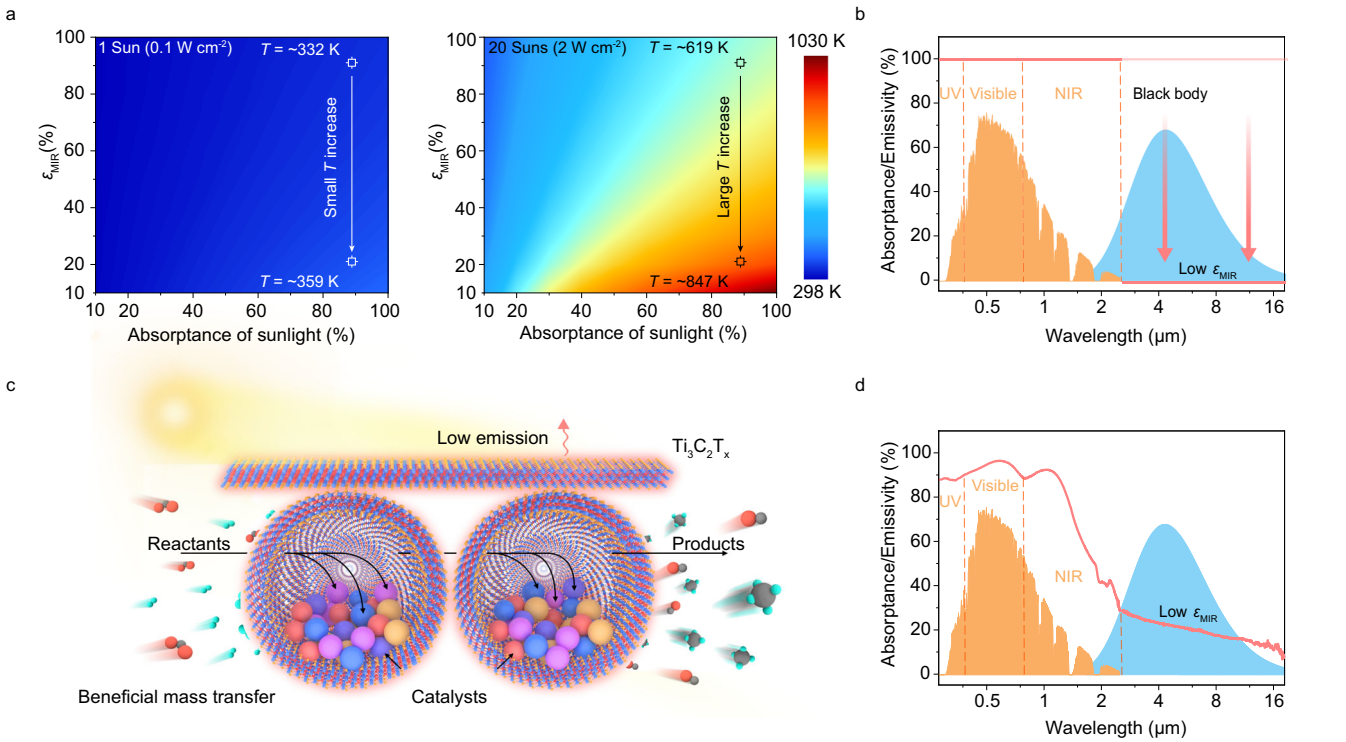

Fig. 1 | The engineered optically selective Janus design. a The simulated temperature at given ε_{MIR} and absorptance of sunlight. At high light power, ε_{MIR} plays a decisive role in the obtained temperature. **b** Schematic of depressing ε_{MIR} to obtain an ideal photothermal catalyst with both broadband and selective spectrum, as well as the AM 1.5 G solar spectrum and the radiation spectrum of a blackbody at 673 K. **c** Schematic of nanoparticles loaded within macroporous $Ti_3C_2T_x$ as catalysts for photothermal catalysis. The flat $Ti_3C_2T_x$ flakes depress ε_{MIR}, meanwhile, the porous structure facilitates the mass transfer of reactants, thus the designed catalyst effectively drives the photothermal catalysis process. **d** The selective spectrum of engineered optically selective catalyst, as well as the AM 1.5 G solar spectrum and the radiation spectrum of a blackbody at 673 K.

https://doi.org/10.1038/s41467-024-51896-4

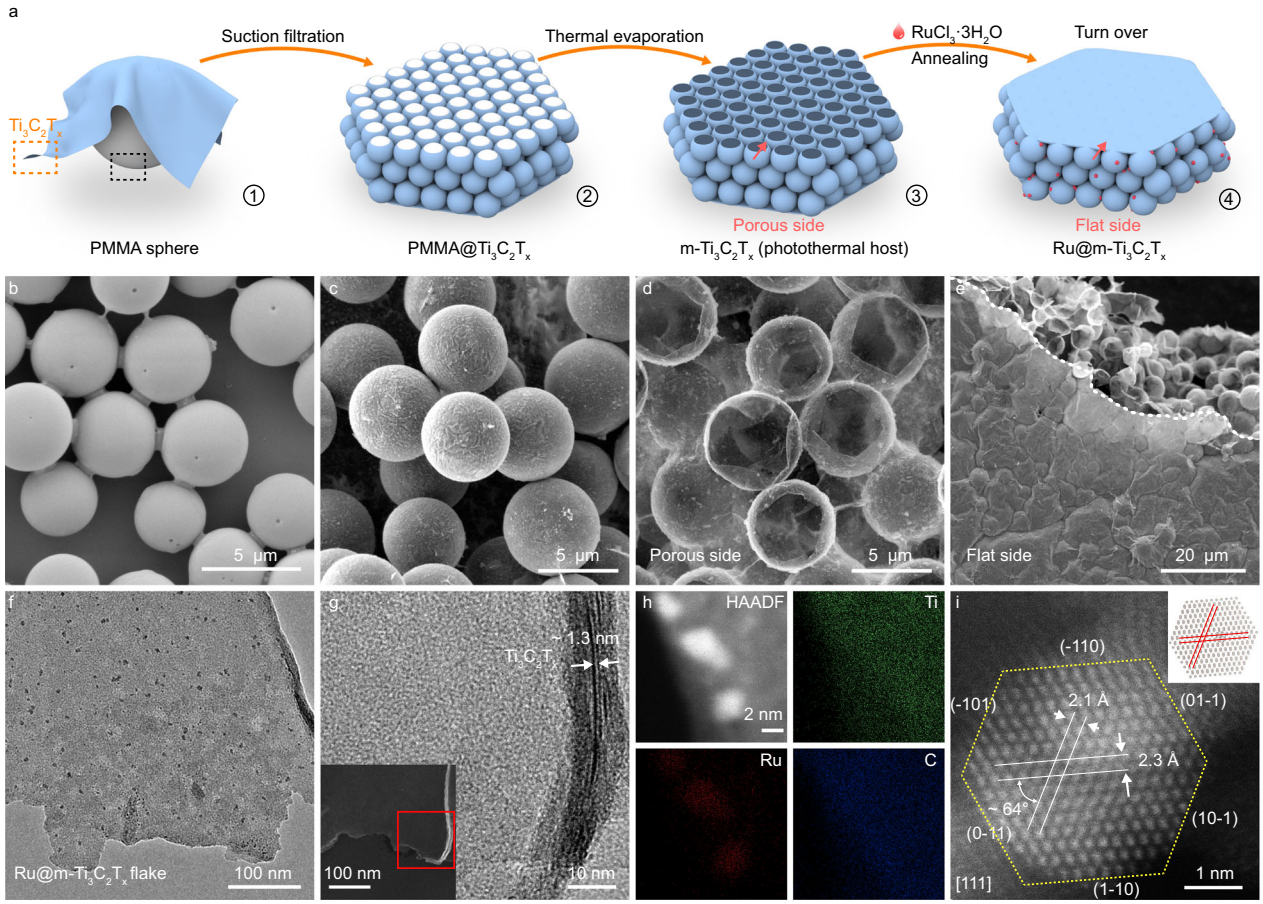

Fig. 2 | Characterizations of designed photothermal host and Ru-loaded MXene catalyst (Ru@m-$Ti_3C_2T_x$). a Schematic of the preparation process of Ru@m-$Ti_3C_2T_x$. **b**–**e** SEM image of PMMA (**b**), PMMA@$Ti_3C_2T_x$ (**c**) and m-$Ti_3C_2T_x$ (**d**, **e**). **f** TEM image of Ru@m-$Ti_3C_2T_x$. **g** HRTEM image of Ru@m-$Ti_3C_2T_x$ and secondary electron image (inset). **h** HAADF-STEM image and corresponding elemental mapping images of Ru@m-$Ti_3C_2T_x$. **i** High-resolution HAADF-STEM image of a single Ru nanoparticle and the corresponding crystalline structure (inset).

products is crucial for photothermal catalytic process, the PMMA spheres were first wrapped by $Ti_3C_2T_x$ flakes via polar groups. Subsequently, PMMA spheres were removed through thermal evaporation to obtain a macroporous $Ti_3C_2T_x$ (m-$Ti_3C_2T_x$) membrane, which contains numerous channels or porosities (Fig. 2b–e and Supplementary Figs. 2–7). After loading the Ru nanoparticle catalyst, we can finally achieve the Ru@m-$Ti_3C_2T_x$ with a porous side composited of macroporous $Ti_3C_2T_x$ spheres and a flat side of $Ti_3C_2T_x$ flakes (thickness ~70 μm, Supplementary Fig. 8).

To characterize the designed photothermal host and the catalyst Ru@m-$Ti_3C_2T_x$, several measurements were performed. Inductively coupled plasma optical emission spectroscopy (ICP-OES) result reveals that the Ru content is ~0.75 wt%, which causes the diffraction peaks associated with metallic Ru could not be detected by X-ray diffraction (XRD) (Supplementary Fig. 6)[37]. The Ru 3*d* and Ru 3*p* peaks were clearly revealed by X-ray photoelectron spectroscopy (XPS), which confirms the presence of Ru in Ru@m-$Ti_3C_2T_x$ (Supplementary Fig. 9)[38]. Figure 2f depicts the transmission electron microscopy (TEM) image of a typical Ru-$Ti_3C_2T_x$ flake. The black dots are uniformly distributed on $Ti_3C_2T_x$ flakes, which are Ru-particles prepared by the impregnation method. The high-resolution transmission electron microscopy (HRTEM) image at the edge of the layer indicates the lattice fringe spacing of ~1.3 nm, in agreement with the (002) plane of $Ti_3C_2T_x$ (Fig. 2g). Meanwhile, the high-angle annular dark field scanning transmission electron microscopy (HAADF-STEM) image and corresponding elemental mappings confirm that C and Ti elements are distributed throughout the support while Ru mainly exists in the form of nanoparticles (Fig. 2h). To reveal the crystal structure, we further investigated a single Ru nanoparticle. The HAADF-STEM image shows that the distances between adjacent planes are 2.3 and 2.1 Å, corresponding to the lattice spacing of the (1-10) and (10-1) planes of metallic Ru, respectively. The result is consistent with the hexagonal close-packing crystal phase of Ru, thus the Ru nanostructures via this preparation process are considered to be crystalline Ru nanoparticles (Fig. 2i). Meanwhile, we probed the flat side of the Ru@m-$Ti_3C_2T_x$ and the Ru@$Ti_3C_2T_x$ catalyst, and we found that the Ru nanoparticle sizes on both sides typically fall within the range of 3–4 nm (Supplementary Figs. 10, 11). Of note, different metal nanoparticles can also be loaded onto our designed $Ti_3C_2T_x$ host using a similar preparation method (see "Method" section for details) for different reactions.

Detailed analysis of its unique photothermal effect

To verify the enhanced photothermal effect from low ε_{MIR} in the designed Ru@m-$Ti_3C_2T_x$ membrane, a detailed analysis of the relationship among surface structure–spectrum–thermal was performed. Specifically, the spectral features of Ru@m-$Ti_3C_2T_x$ strongly depend on the surface structure irradiated under sunlight, which could be identified by the crystal orientations of nanoflakes[33,39]. On the flat side, the overall ε_{MIR} of m-$Ti_3C_2T_x$ (2.8–18.3 μm) is only ~21%, which remarkably prohibits it from thermal radiation loss, thus promoting localized high temperature on this side of the designed catalyst (Fig. 3a). Typically, as a two-dimensional material, the multilayer overlapping structure of $Ti_3C_2T_x$ forms the crystallographic orientation of a certain characteristic crystal plane (002), which can be

https://doi.org/10.1038/s41467-024-51896-4

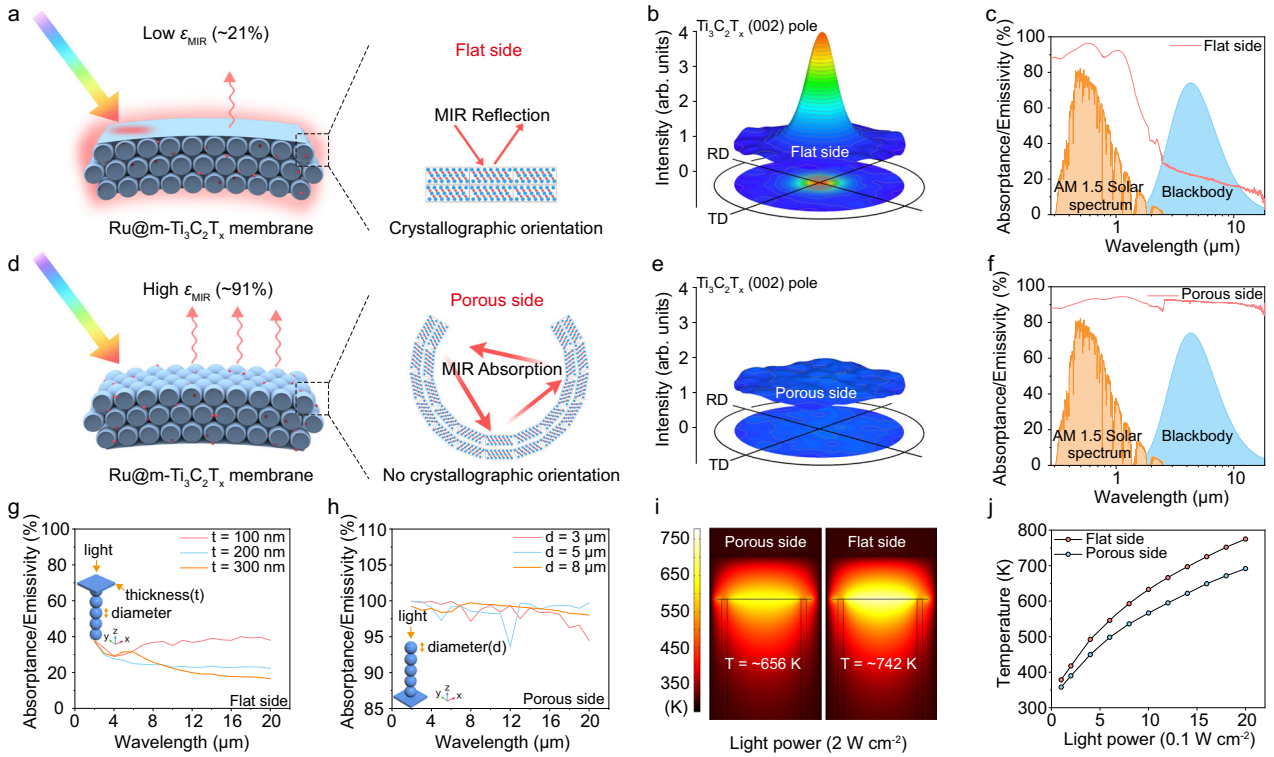

Fig. 3 | Comparison of different photothermal effects caused by two different side structures. a Schematic of the high photothermal effect of the flat side due to the low ε_{MIR} (~21%). **b** The $Ti_3C_2T_x$ (002) pole figure for the flat side of m-$Ti_3C_2T_x$. **c** The spectrum of the flat side of m-$Ti_3C_2T_x$ within the 0.28–18.3 μm wavelength range, as well as the AM 1.5 G solar spectrum and the radiation spectrum of a blackbody at 673 K. **d** Schematic of the low photothermal effect of the porous side due to the high ε_{MIR} (~91%). **e** The $Ti_3C_2T_x$ (002) pole figure for the porous side of m-$Ti_3C_2T_x$. **f** The spectrum for the porous side of m-$Ti_3C_2T_x$ within the 0.28–18.3 μm wavelength range, as well as the AM 1.5 G solar spectrum and the radiation spectrum of a blackbody at 673 K. **g** The spectrum simulation for the flat side of m-$Ti_3C_2T_x$ with varying thicknesses within the 0.28–20 μm wavelength range. **h** The spectrum simulation for the porous side of m-$Ti_3C_2T_x$ with varying pore diameters within the 0.28–20 μm wavelength range. **i** The thermal simulations of different sides. **j** The measured temperatures from infrared images under different light powers.

determined by X-ray pole figure[40,41]. For this measurement, the 2θ value was fixed and the m-$Ti_3C_2T_x$ membrane was rotated from 0° to 360° at series of tilt angles from 0° to 75°. Figure 3b and Supplementary Fig. 12a show a (002) pole figure for the flat side of m-$Ti_3C_2T_x$, with one spot at a tilt angle of 0°. The out-of-plane orientation of flat side was detected, corresponding to the (002) plane. In this orientation, similar to the natural crystalline structure of $Ti_3C_2T_x$, the flat side of the m-$Ti_3C_2T_x$ membrane shows an excellent spectral selectivity, which exhibits an 88% absorptance in the sunlight wavelength range and a ε_{MIR} of 21% (Fig. 3c).

To further demonstrate the low ε_{MIR} on the flat side, we also performed the full-wave simulation using the finite-element method-based software package COMSOL Multiphysics (see Method for details). In the calculation model, periodic close-packing $Ti_3C_2T_x$ spherical pores are used for simplicity. We used the permittivity data of $Ti_3C_2T_x$ from previous work[33]. Meanwhile, we characterized the thickness of the top layer to be ~150 nm (Supplementary Fig. 13). Calculated emissivity spectra at the normal incidence for flat side with different pore diameters are shown in Fig. 3g and Supplementary Fig. 14. The relatively low ε_{MIR} is nearly independent with pore diameters. The phenomenon can be explained by the large real and imaginary permittivity of $Ti_3C_2T_x$. The infrared light is highly reflected from the top flat side due to the drastic impedance mismatching between reactant gas and $Ti_3C_2T_x$ slabs, and the large imaginary permittivity of $Ti_3C_2T_x$ also leads to the strong absorption of residual light even with hundreds of nanometers-thick slabs. As a result, light can hardly transmit to the porous $Ti_3C_2T_x$ layer, and the low ε_{MIR} is nearly unchanged with different diameters of $Ti_3C_2T_x$ pores.

Furthermore, to understand the attenuation of the photothermal effect of conventional photothermal catalysts from high ε_{MIR}, the irradiated surface was experimentally reconstructed. As we all know, multiple scattering is a common phenomenon in optics, which increases emissivity at the corresponding waveband. The porous side which consists of massive ~5 μm macroporous $Ti_3C_2T_x$ spheres increase the ε_{MIR} via multiple scattering, providing an in-situ control group (Fig. 3d). According to the (002) pole figure for the porous side of m-$Ti_3C_2T_x$, there is non-orientation on the porous side (Fig. 3e and Supplementary Fig. 12b). It could be caused by the large angular bending of the $Ti_3C_2T_x$ flakes. Figure 3f shows that the overall ε_{MIR} for the porous side of m-$Ti_3C_2T_x$ (2.8–18.3 μm) rises to ~91%, which significantly increases the thermal emission. According to the simulation, strongly enhanced ε_{MIR} is found for porous side. The near-unity ε_{MIR} is due to the multiple scattering effect generated in $Ti_3C_2T_x$ pore layers (Fig. 3h). Although the shell of a single pore is thick, the multiple scattering effect effectively increases the time and strength of light-matter interaction, leading to near-unity and broadband emission in infrared wavelengths. As a result, the engineered porous side of the m-$Ti_3C_2T_x$ membrane possesses no crystal orientation and exhibits high emission characteristics in the 0.28–18.3 μm wavelength range, with an absorptance of 92% in the sunlight wavelength range and an ε_{MIR} increasing to 91% (Fig. 3f).

To further verify the enhanced photothermal effect from low ε_{MIR}, light–thermal conversion efficiency calculation, infrared images, and thermal simulation were employed to demonstrate the reduction of thermal loss. Benefit from the low ε_{MIR}, the light–thermal conversion efficiency ($\eta_{light\text{-}th}$, at 698 K) of the flat side can reach a high value of

74.2% far higher than that of the porous side (32.2%) (details seen in Methods). This difference will be more obvious in the high-temperature region, as mentioned above. Under 2 W cm^{-2} light power, the highest temperatures at the center of the flat side can reach 742 K, while the porous side only reaches 656 K (Fig. 3i). This similar phenomenon also can be observed under other light powers. The temperature difference between the two sides increases with the light power (Supplementary Fig. 15). Furthermore, the infrared images also prove the temperature difference between the two different sides, and this difference also increases with the light power (Fig. 3j and Supplementary Fig. 16). The flat side of Ru@m-$Ti_3C_2T_x$ possess higher heating rate than the porous side of Ru@m-$Ti_3C_2T_x$ (Supplementary Fig. 17). Meanwhile, to systematically assess the photothermal process of the catalyst, we performed experiments and simulations to investigate the its cooling process. As a result, the cooling rate of the flat side of Ru@m-$Ti_3C_2T_x$ is lower than that of the porous side of Ru@m-$Ti_3C_2T_x$ in the high-temperature region, which attributes to the reduction of thermal radiation loss (Supplementary Figs. 18, 19 and Supplementary Note 3). The heat profile is also investigated to prove the uniform distribution of heat in the architecture (Supplementary Fig. 20 and Supplementary Note 4). Through the detailed analysis of surface structure–spectrum–thermal, it reveals that the enhanced photothermal effect originates from low ε_{MIR} on the flat side of the Ru@m-$Ti_3C_2T_x$ membrane, which could serve as an ideal photothermal catalyst.

Boosting photothermal catalytic performance

This photothermal host design, composited of macroporous $Ti_3C_2T_x$ spheres and $Ti_3C_2T_x$ flakes, aims to enhance the photothermal effect via low ε_{MIR} and to provide channel for the mass transfer of reactants and products. To reveal the advantages of our catalyst design, CO_2 hydrogenation performance was tested under full-Arc Xe lamp irradiation for the Ru@m-$Ti_3C_2T_x$ membrane. $Ti_3C_2T_x$ membrane and Ru@$Ti_3C_2T_x$ membrane were also prepared and used as references (see Method for details). First, to clarify whether the photothermal host affects the Sabatier reaction, a series of control experiments were performed under light power 0.1–2 W cm^{-2} for pure $Ti_3C_2T_x$ membrane. At different light powers, nearly no methane and intermediates can be detected, clearly indicating that $Ti_3C_2T_x$ itself is not active to CO_2 methanation (Supplementary Figs. 21–23). As shown in Supplementary Fig. 24, the catalytic activity of the Ru@$Ti_3C_2T_x$ membrane increases with the light power. However, its CH_4 production rate normalized by the mass of Ru only reached 128.5 mmol g_{Ru}^{-1} h^{-1} at 2 W cm^{-1}, which could result from insufficient contact of the reactant with the Ru catalyst. In sharp contrast, the porous side of Ru@m-$Ti_3C_2T_x$ (Ru@m-$Ti_3C_2T_x$-p) membrane, despite having higher ε_{MIR}, possesses much higher CH_4 production rate (the average value of 733.2 mmol g_{Ru}^{-1} h^{-1} at 2 W cm^{-1}) at each light power compared with Ru@$Ti_3C_2T_x$ membrane, which could be attributed to rapid mass transfer of reactants as well as products (Fig. 4a, the blue line). The contribution of mass transfer has been further verified by simulation and in-situ diffuse reflectance infrared Fourier transform spectroscopy (DRIFTS) (Supplementary Figs. 25–29, Supplementary Table 4 and Supplementary Note 5).

Furthermore, the reduction of the ε_{MIR} can increase the photothermal effect and further improve the methane yield of photothermal CO_2 reduction. As shown in Fig. 4a, the red line, catalytic activity based on the flat side of the Ru@m-$Ti_3C_2T_x$ (Ru@m-$Ti_3C_2T_x$-f) increases with the light power, which outperforms Ru@$Ti_3C_2T_x$ and Ru@m-$Ti_3C_2T_x$-p under all light powers, especially at high intensities. Under the highest power of 2 W cm^{-2}, the average CH_4 production rate of Ru@m-$Ti_3C_2T_x$-f reaches 3317.2 mmol g_{Ru}^{-1} h^{-1}, which is over 4 times higher than that of Ru@m-$Ti_3C_2T_x$-p (Supplementary Fig. 30). On the other hand, to achieve the same production rate (733.2 mmol g_{Ru}^{-1} h^{-1}), Ru@m-$Ti_3C_2T_x$-f could reduce about 0.4 W cm^{-2} power compared with that of Ru@m-$Ti_3C_2T_x$-p at 2 W cm^{-2}. Furthermore, the high product selectivity for CH_4 can be detected on both Ru@m-$Ti_3C_2T_x$-p and Ru@m-$Ti_3C_2T_x$-f, probably due to the same size of Ru nanoparticles which does not vary with the irradiated surface (Fig. 4b, c)[42]. In order to eliminate potential differences in catalytic activity due to the placement state of the catalysts, the Arrhenius plots of Ru@m-$Ti_3C_2T_x$-p and Ru@m-$Ti_3C_2T_x$-f were constructed to assess kinetic performance. The results demonstrate that no noticeable changes were observed in the apparent activation energies (E_a) of these two sides of catalysts, indicating that the reaction energy remains unchanged with the placement state (79.8 ± 4.2 kJ mol^{-1} for Ru@m-$Ti_3C_2T_x$-p and 76.5 ± 8.6 kJ mol^{-1} for Ru@m-$Ti_3C_2T_x$-f) (Supplementary Fig. 31).

To demonstrate the high stability of our catalyst with the proposed design, we first performed 20-h consecutive testing and another 10-h consecutive testing for Ru@m-$Ti_3C_2T_x$-f (Fig. 4d). Between the two tests, the Ru@m-$Ti_3C_2T_x$-f was kept in argon gas at room temperature for two months. During the first 20-h test, both the CO_2 conversion rate and product selectivity are almost no change. Surprisingly, the next 10-h test still exhibits stable selectivity in spite of the slightly fluctuating yield of CH_4. The stable activity and selectivity can be attributed to the fact that the strong physical barrier between $Ti_3C_2T_x$ layers resists the Ostwald ripening of Ru nanoparticles (see following post-catalysis characterizations). As shown in Supplementary Fig. 32, the hollow structure of Ru@m-$Ti_3C_2T_x$ is nearly not changed and the overall structure was kept intact after 30 cycles of testing. Meanwhile, the absorptance of visible light still reaches 87.4%, and the emissivity in the mid-infrared region remains at 22.0% (Supplementary Fig. 33). Besides, the Ru nanoparticle still possesses good crystallinity and high dispersion, and its combination with the $Ti_3C_2T_x$ has no obvious change (Supplementary Figs. 34, 35). The high stability may attribute to the demonstrated structural stability of the MXene analogue and the potential interaction between nanoparticle and $Ti_3C_2T_x$[43,44]. We compared the CH_4 production rate to typical reports of CO_2 methanation with or without an external heater (Fig. 4e and Supplementary Table 5). The results indicate that, at high optical power levels, whether based on the mass of Ru or the entire catalyst, our catalyst exhibits significantly higher production rates compared to the reported works, and it achieves a yield record among catalysts without active supports.

Our generic design strategy is expected to serve the vast majority of photothermal catalytic reactions. In order to prove the efficient catalysis performance resulting from the reduction of the ε_{MIR}, Pd, and Ni catalysts were also loaded on to m-$Ti_3C_2T_x$ as active metal catalysts. The low yields are obtained compared with Ru-based catalysts, which ascribed to the types of active metals testified by previous works[15]. However, both catalysts have several times the performance improvement reaching an excellent yield by the reduction of the ε_{MIR} without active supports (Fig. 4g). Furthermore, to demonstrate the generality of the Janus design towards various MXene materials, we also performed structural design on two other MXene, i.e. Ti_3CNT_x and Ti_2CT_x. As a result, both materials exhibit excellent selective spectra and complete porous structures (Supplementary Figs. 36, 37).

To confirm the origin of the as-produced CH_4, the ^{13}C isotope labeling experiment was performed for the photothermal hydrogenation. The products were examined by gas chromatography-mass spectrometry (GC–MS). A major signal at a mass/charge ratio of 17 on the mass spectrum corresponding to $^{13}CH_4$ appears, which verifies that the as-detected CH_4 originates from the CO_2 hydrogenation process (Supplementary Fig. 38). We also performed in-situ DRIFTS under reaction conditions to reveal the possible reaction mechanism of CO_2 methanation on our Ru@m-$Ti_3C_2T_x$. The measurements were performed at 300 °C in the reaction gas mixture of 80 vol% H_2/20 vol% CO_2. As shown in Fig. 4f and Supplementary Fig. 39, the peak at 1649 cm^{-1} is characteristic of surface CO_2^* species, namely bicarbonate[45,46]. As the reaction proceeded, the formate species

https://doi.org/10.1038/s41467-024-51896-4

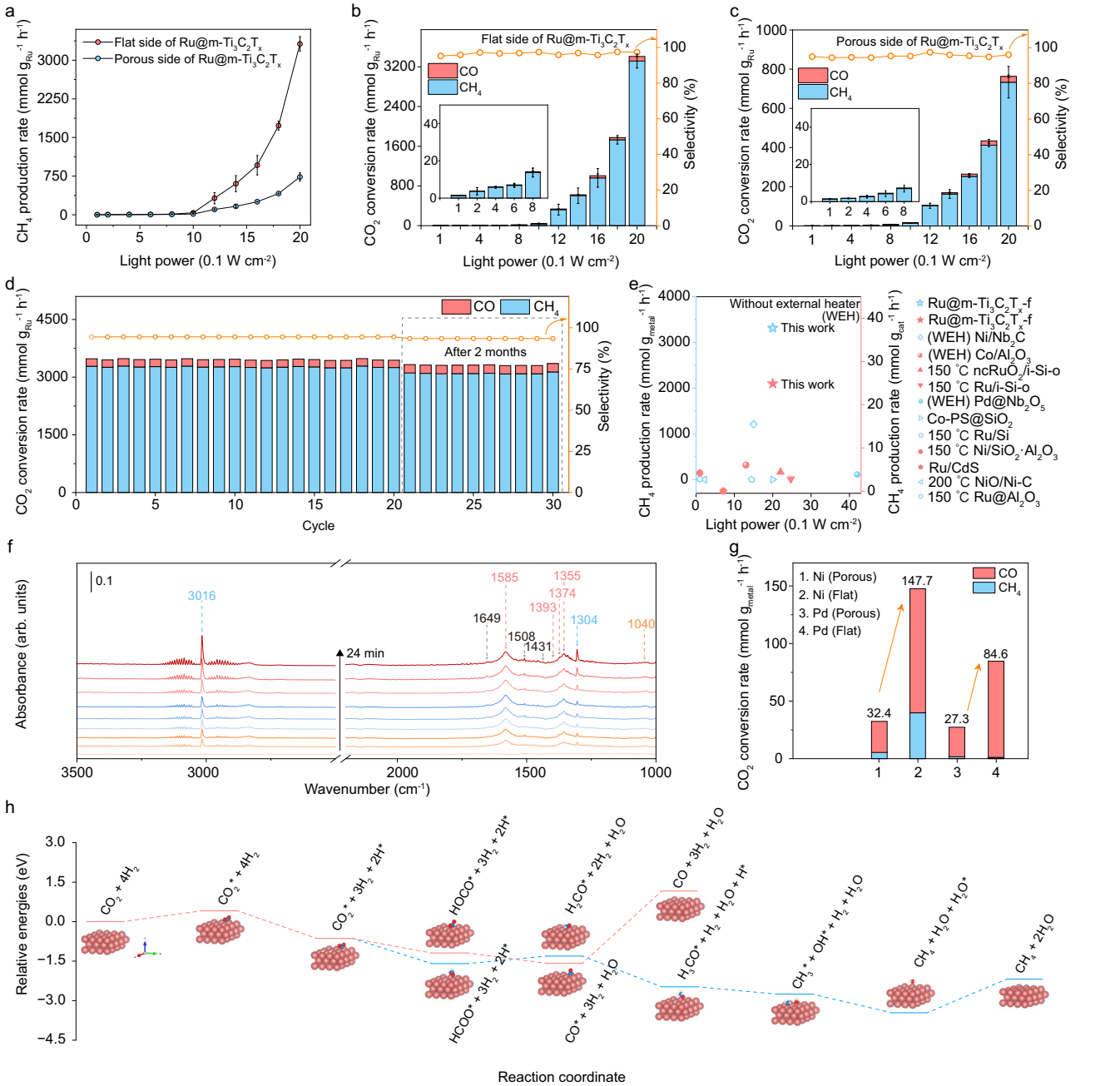

Fig. 4 | Photothermal catalytic performance of the designed optically spectral catalyst and mechanism analysis. a CH_4 production rate on the two different sides of the Ru@m-$Ti_3C_2T_x$ catalyst. **b** CO_2 conversion rate and selectivity on the flat side of the catalyst. **c** CO_2 conversion rate and selectivity on the porous side of the catalyst. **d** Stability test for hydrogenation of CO_2 at 2 W cm^{-2} without external heating. **e** Performance comparison of CO_2 reduction among this work and previous works. **f** In-situ DRIFTS over flat side of Ru@m-$Ti_3C_2T_x$. **g** CO_2 conversion rate on other catalysts with our design strategy. **h** Energy landscape for CO_2 hydrogenation to CO and CH_4 on the typical (0001) surface of Ru particles. To improve legibility, H_2 is omitted from the labels after the initial state. All error bars represent the standard deviations of three independent measurements and the bars indicate mean values.

gradually emerged according to the peaks at 1585, 1393, 1374, and 1355 cm^{-1}, which means the transformation of bicarbonate to formate[47,48]. Meanwhile, the peak at 1040 cm^{-1} for CH_3O^* is detected, demonstrating the further hydrogenation of HCOO*. Consequently, the signal intensities attributed to CH_4 species (located at 3016 and 1304 cm^{-1}) increased gradually as the reaction progressed. The peak assignments of the surface species are listed in Supplementary Table 6. The reaction diagram of CO_2 hydrogenation on the (0001) surface of Ru was explored by using density functional theory (DFT) calculations to further reveal the reaction mechanisms (Fig. 4h)[49,50]. The adsorption and conversion of CO_2 on the Ru site are more favorable than other sites. Although both reactions $CO_2^* + H^* \rightarrow HOCO^*$ and $CO_2^* + H^* \rightarrow HCOO^*$ are exothermic. The reaction $CO_2^* + H^* \rightarrow HCOO^*$ ($\Delta_r G = -0.956$ eV) is energetically more preferred than $CO_2^* + H^* \rightarrow HOCO^*$ ($\Delta_r G = -0.555$ eV). So, we conclude that HCOO* is the dominating species of CO_2 reduction on Ru surface, which is in consistent with the in-situ DRIFTS observations. Whereafter, the C-O bond cleavage of HOCO* and the subsequent desorption at the catalytic site render the entire process highly energetically unfavorable ($\Delta_r G = 2.355$ eV). In sharp contrast, the C-O bond cleavage of HCOO*, followed by its successive hydrogenation until the final formation of CH_4, results in the entire process highly energetically favorable

($\Delta_r G = -0.989$ eV), which is also consistent with the in-situ DRIFTS observations. Therefore, it can be inferred that CO_2 hydrogenation on the surface of Ru exhibits good selectivity towards CH_4.

Discussion

In summary, we demonstrated an optically selective catalyst based on 3D $Ti_3C_2T_x$ structures, which possess low ε_{MIR}, high α_{light}, and fast mass transfer kinetics. $Ti_3C_2T_x$ flakes with high in-plane permittivity in the mid-infrared enable the ideal ε_{MIR} to reduce the thermal emission of catalysts, while the designed 3D porous structure composed of $Ti_3C_2T_x$ spheres provides numerous channels for mass transfer of reactants/products. In addition, this universal architecture can be integrated with various nanoparticle catalysts for a wide range of reactions. Taking Sabatier reaction and RWGS as demonstrations, we achieved around 3 times and 4 times improvement in yield for CH_4 and CO compared to that without this design, respectively. The CO_2 methanation yield reaches 3317.2 mmol g_{Ru}^{-1} h^{-1} at a light power of 2 W cm^{-2}, setting a performance record among catalysts independent of active supports. We believe that the design of the optically selective catalyst not only provides a new route for the reduction of CO_2 in photothermal catalysis but also facilitates various photothermal-driven chemical reactions toward green chemistry.

Methods

Preparation of $Ti_3C_2T_x$ membrane

According to the previous work, the preparation of $Ti_3C_2T_x$ includes five steps[30]. First, 2 g lithium fluoride and 40 mL hydrochloric acid were stirred in a Teflon beaker (100 mL) for 30 min. Second, 2 g MAX-Ti_3AlC_2 powder was added to the above solution, and the reaction temperature was adjusted to 35 °C, and kept this temperature for 24 h. Third, the obtained reaction liquid was divided into four parts for centrifugation (959 × *g*), and then the supernatant was discarded. 40 mL deionized water was added into four portions of precipitate, and they were thrown into high-power ultrasonic machine (750 W) for 10 min. The process was repeated by several times until the pH of the supernatant reached 5. Fourth, 40 mL ethanol was added to each precipitate, followed by ultrasound for 1 h (this will facilitate the separation of the layered $Ti_3C_2T_x$), followed by centrifuged (7826 × *g*), and the precipitate was collected. Finally, 20 mL deionized water was added into four portions of precipitate followed by ultrasonication (750 W, 20 min) and centrifugation (959 × *g*), and the black supernatant was collected as a few-layer $Ti_3C_2T_x$ dispersion (the specific concentration can be adjusted by adding deionized water). The $Ti_3C_2T_x$ membrane could be obtained via filtering as-prepared 20 mL few-layer $Ti_3C_2T_x$ dispersion (1 mg mL^{-1}). In addition, the Ti_3CNT_x and Ti_2CT_x were prepared in a similar method using MAX-Ti_3AlCN and MAX-Ti_2AlC as precursors, respectively.

Preparation of PMMA sphere

According to the previous work, the preparation of ~5 μm PMMA spheres is through a typical dispersion polymerization process[36]. Primarily, 50 mL of methanol, 118.4 mg of azobisisobutyronitrile, and 1.578 g of polyvinyl pyrrolidone (PVP, molecular weight of 58,000) were added sequentially to a 100 mL flask and stirred to dissolve. Subsequently, the argon was pumped into the solution for 3–4 min to fill the flask with a protective atmosphere. Finally, 4.383 mL methyl methacrylate and a stirrer were added to the flask, and the polymerization was carried out with magnetic stirring at 55 °C for 24 h. PMMA spheres can be stored after cleaning with methanol.

Preparation of Ru@m-$Ti_3C_2T_x$, Ru@$Ti_3C_2T_x$, Pd@m-$Ti_3C_2T_x$, Ni@m-$Ti_3C_2T_x$, m-Ti_2CT_x and m-Ti_3CNT_x

The preparation of Ru@m-$Ti_3C_2T_x$ mainly consisted of two processes: a hard template method and further an impregnation method[34]. First, as-prepared 20 mL few-layer $Ti_3C_2T_x$ dispersion (1 mg mL^{-1}) and 40 mL PMMA sphere dispersion (2 mg mL^{-1}, dispersed by deionized water) were stirred in a 100 mL flask for 24 h. Note that the induced electrostatic self-assembly effect comes from the surface functional groups of $Ti_3C_2T_x$ and PMMA. Next, the PMMA@$Ti_3C_2T_x$ membrane was obtained by suction filtration and further annealed in flowed argon (100 sccm) at 500 °C to form an m-$Ti_3C_2T_x$ membrane. Here, the m-Ti_2CT_x and m-Ti_3CNT_x can be synthesized using a similar method by replacing $Ti_3C_2T_x$ with Ti_2CT_x and Ti_3CNT_x, respectively. Finally, the $RuCl_3{\cdot}3H_2O$ solution was added dropwise to $Ti_3C_2T_x$ membrane support and m-$Ti_3C_2T_x$ membrane support and annealed at 350 °C under mixture gas (10% H_2 and 90% Ar) for 1 h to obtain Ru@$Ti_3C_2T_x$ and Ru@m-$Ti_3C_2T_x$, respectively. Palladium and nickel are also loaded by a method similar to those described above. $PdCl_2$ and $NiCl_2$ are the sources of palladium and nickel, respectively.

Characterization

XRD was performed on a Bruker D8 X-ray diffractometer with Cu Kα radiation. BET was performed on a Micromeritics ASAP 2460. SEM images were obtained by Tescan MIRAS3 SEM. TEM images were obtained with a Talos F200E TEM. The UV wavelength range in the 0.28–2.5 μm range was measured by ultraviolet-visible spectroscopy (UV-3600, Shimadzu) with an attached integrating sphere (ISR-3100). The NIR wavelength within the 2.5–18.3 μm range was measured by an FTIR spectrometer (Nicolet IS50, ThermoFisher) equipped with a gold integrating sphere (IntergatIR MIR, Pike). In-situ FTIR spectra were measured by an FTIR spectrometer (Nicolet IS50, ThermoFisher) equipped with a reaction tank (Hefei In-situ Technology). TGA was performed on a TG/DTA7300 (Seiko In.). The elemental valence states were investigated by X-ray photoelectron spectroscopy (Thermo Scientific K-Alpha). The invisible temperature data was collected via coaxial laser infrared thermometer. The infrared images were taken using a FLUKE Tix 580 infrared camera. The Ru content was measured on an Agilent 5110 ICP-OES spectrometer.

Structural optical simulation

All calculations are performed using the finite-element method (FEM) based software package COMSOL Multiphysics. In the simplified calculation model, three-dimensional square close-packing MXene spherical pores with an equal diameter and a MXene slab layer are used, see the schematic view of a unit cell in Fig. 3g, the number of MXene spherical pores along the z-direction is dependent on the total thickness (60-70 μm) and pore diameters. The shell thickness of MXene pores is 8 nm. The periodic boundary condition is used along x- and y- directions. Two ports at the top (reflection plane) and the bottom surfaces (transmission plane) of the FEM model are used for calculating the reflectivity (R) and the transmissivity (T), the absorptivity (A) or emissivity (E) is defined as A(E) = 1-R-T. The distance between ports and adjacent MXene structures is larger than the calculated wavelength. To simulate the ultrathin shell of pores, the transition boundary condition with an 8-nm thickness is utilized for each MXene pore. Free tetrahedral meshing with a maximum size of 1 μm is adopted for pores and adjacent air volumes. Swept meshes with 5 distributions and 40 distributions are utilized for the slab region and the air volume at both ends, respectively.

Thermal-field simulation

The thermal-field simulation is through COMSOL Multiphysics® software. The size and structure of the reactor in the simulation are the same as that in the experiment, which is shown in Supplementary Fig. 40. The heat source, whose power density (P_{in}) is set from 0.1 to 2 W cm^{-2}, is added above the material to simulate solar radiation used in the experiment. The solar-radiation absorption of the catalyst is simulated by multiplying the P_{in} by the measured absorptivity (0.88 and 0.92) in the visible band. The thermal emission of the catalyst is simulated by the surface-to-surface-radiation module, where the

emissivity of the catalysts is set to 0.21 and 0.91, respectively. The heat-transfer-in-solid module is used to simulate the thermal convection between the reactor and the external environment with a heat transfer coefficient of 5 $W m^{-2} K^{-1}$, where the temperature of the external environment is fixed at 293.15 K. The reactor body is defined as AISI 316 L stainless steel with 18.4 $W m^{-1} K^{-1}$ thermal conductivity, 7980 $kg m^{-3}$ density, and 502 $J kg^{-1} K^{-1}$ constant pressure specific heat capacity. The optical window is defined as Sapphire crystal with 42.5 $W m^{-1} K^{-1}$ thermal conductivity, 4000 $kg m^{-3}$ density, and 780 $J kg^{-1} K^{-1}$ constant pressure specific heat capacity. The solid support is defined as quartz with 1.4 $W m^{-1} K^{-1}$ thermal conductivity, 2210 $kg m^{-3}$ density, and 730 $J kg^{-1} K^{-1}$ constant pressure specific heat capacity.

Light–thermal conversion efficiency calculation

The spectrally averaged sunlight absorption (α_{light}) is defined as:

$$\alpha_{light} = \frac{\int I_{light}(\lambda)\alpha(\lambda)d\lambda}{I_{light}} \quad (2)$$

The spectrally averaged thermal emissivity is calculated by

$$\varepsilon_{MIR}(T) = \frac{\int I_{BB}(T,\lambda)\varepsilon(\lambda)d\lambda}{\sigma T^4} \quad (3)$$

Hence, the light–thermal energy conversion efficiency can be obtained by[29]

$$\eta_{light-th}(T) = \alpha_{light} - \varepsilon_{MIR}\frac{\sigma(T^4 - T_0^4)}{I_{light}} \quad (4)$$

Here, $I_{light}(\lambda)$, $I_{BB}(T, \lambda)$, $\alpha(\lambda)$ and $\varepsilon(\lambda)$ represent the light power, energy distribution under the radiation spectrum of a blackbody at a given temperature T, and absorptance and the emissivity at the wavelength λ, respectively. And σ is the Stefan–Boltzmann constant, T is the operating temperature, and T_O is the ambient temperature.

Computational methods

We explored the origin of the as-produced CH_4 by calculating various different reaction pathways. All the structures were optimized by the density functional theory (DFT) calculations as implemented in the Vienna Ab initio Simulation Package (VASP)[51,52]. The interaction between valence electrons and ion cores were accurately described using the projector-augmented wave (PAW) method[52,53]. The Perdew-Burke-Ernzerhof (PBE) exchange-correlation functional[54,55] was adopted to treat the interaction between valence electrons. The DFT-D2 method[56] was used to describe the van der Waals interaction between molecules and Ru (0001) substrate. We used a plane wave basis set with an energy cutoff of 450 eV in the calculations. All the structures were fully relaxed, and the convergence criteria for energy and force were set at 10^{-5} eV and 10^{-4} eV/Å, respectively. The relative energy $\Delta_r G$ of the two systems was obtained from $\Delta_r G = G_1 - G_2$, where G_2 is the Gibbs free energy of the second system, G_1 is the Gibbs free energy of the first system.

CO_2 hydrogenation measurements

The gas-phase CO_2 hydrogenation experiments were conducted in a batch reactor (100 mL) with internal gas circulation (CEL-HPR, CEAULight). In the CO_2 hydrogenation tests, ~4 mg of catalyst membrane was placed on a hollowed-out shelf. Ru loading mass is around 0.75 wt%. The infrared images were taken using a FLUKE Tix 580 infrared camera. A 300 W Xe lamp (PLS-SXE300D, Beijing Perfect light) was used to drive photothermal CO_2 hydrogenation. The reactor is cleaned by bubbling and evacuating the mixture of CO_2 and H_2 (1:4) thrice. Subsequently, when the injection pressure reached 4 bar, the reactor was sealed, the Xe lamp was turned on, and the photothermal catalytic reaction began. After the reaction, 1 mL of gas was taken out of the reactor and injected into the gas chromatography (GC-2014, Shimadzu) to detect the composition of the gas (the amounts of CO and CH_4 were analyzed with a flame ionization detector installed in the same GC).

The ^{13}C isotope labeling experiment was also performed in the above reactor with $^{13}CO_2$ (99.9 atom %, Sigma–Aldrich) and H_2. Before the catalytic reaction, the reactor was also degassed and purged with a mixture of $^{13}CO_2$ and H_2 (1:4) thrice to eliminate the interference of impurity gas to the experiment. The ^{13}C isotope product gases were measured using an Agilent 6890 A gas chromatographic mass spectrometer.

The CH_4 production rate (R_{CH4}), CO production rate (R_{CO}) and CO_2 conversion rate (R_{CO2}) were defined as follow:

$$R_{CH4} = \frac{n_{CH4}}{m_{cat}\omega_{Ru}t} \quad (5)$$

$$R_{CO} = \frac{n_{CO}}{m_{cat}\omega_{Ru}t} \quad (6)$$

$$R_{CO2} = R_{CH4} + R_{CO} \quad (7)$$

The selectivity of CH_4 is defined as follow:

$$S_{CH4} = \frac{R_{CH4}}{R_{CH4} + R_{CO}} \quad (8)$$

n is the yield of products (mmol), m_{cat} is the mass of the catalyst (g), ω_{Ru} is the loading percent of Ru, and t is the irradiation time (h).

Data availability

All relevant data are included in the manuscript and Supplementary Information. Source data are provided with this paper.

References

1. Lewis, N. S. & Nocera, D. G. Powering the planet: chemical challenges in solar energy utilization. *Proc. Natl Acad. Sci. USA* **103**, 15729–15735 (2006).
2. Song, C. Q., Wang, Z. H., Yin, Z., Xiao, D. Q. & Ma, D. Principles and applications of photothermal catalysis. *Chem. Catal.* **2**, 52–83 (2022).
3. Jing, J. F., Yang, J., Li, W. L., Wu, Z. H. & Zhu, Y. F. Construction of interfacial electric field via dual-porphyrin heterostructure boosting photocatalytic hydrogen evolution. *Adv. Mater.* **34**, 2106807 (2022).
4. Wang, C. W. et al. Engineered hematite mesoporous single crystals drive drastic enhancement in solar water splitting. *Nano Lett.* **16**, 427–433 (2016).
5. Rao, H., Schmidt, L. C., Bonin, J. & Robert, M. Visible-light-driven methane formation from CO_2 with a molecular iron catalyst. *Nature* **548**, 74–77 (2017).
6. Huang, H. N. et al. Triphase photocatalytic CO_2 reduction over silver-decorated titanium oxide at a gas-water boundary. *Angew. Chem. Int. Ed.* **61**, e202200802 (2022).
7. Zhou, L. N. et al. Light-driven methane dry reforming with single atomic site antenna-reactor plasmonic photocatalysts. *Nat. Energy* **5**, 61–70 (2020).
8. Meng, X. G. et al. Nanometals for solar-to-chemical energy conversion: From semiconductor-based photocatalysis to plasmon-mediated photocatalysis and photo-thermocatalysis. *Adv. Mater.* **28**, 6781–6803 (2016).

9. Ghoussoub, M., Xia, M. K., Dunchesne, P. N., Segal, D. & Ozin, G. Principles of photothermal gas-phase heterogeneous CO_2 catalysis. *Energy Environ. Sci.* **12**, 1122–1142 (2019).
10. Szalad, H., Peng, L., Primo, A., Albero, J. & García, H. Fe clusters embedded on N-doped graphene as a photothermal catalyst for selective CO_2 hydrogenation. *Chem. Commun.* **57**, 10075–10078 (2021).
11. Yang, M. Q., Gao, M. M., Hong, M. H. & Ho, G. W. Visible-to-NIR photon harvesting: progressive engineering of catalysts for solar-powered environmental purification and fuel production. *Adv. Mater.* **30**, 1802894 (2018).
12. Lin, H. W., Luo, S. Q., Zhang, H. B. & Ye, J. H. Toward solar-driven carbon recycling. *Joule* **6**, 294–314 (2022).
13. Luo, S. Q., Ren, X. H., Lin, H. W., Song, H. & Ye, J. H. Plasmonic photothermal catalysis for solar-to-fuel conversion: Current status and prospects. *Chem. Sci.* **12**, 5701–5719 (2021).
14. Chen, G. B. et al. Alumina-supported CoFe alloy catalysts derived from layered-double-hydroxide nanosheets for efficient photothermal CO_2 hydrogenation to hydrocarbons. *Adv. Mater.* **30**, 1704663 (2018).
15. Meng, X. G. et al. Photothermal conversion of CO_2 into CH_4 with H_2 over group VIII nanocatalysts: An alternative approach for solar fuel production. *Angew. Chem. Int. Ed.* **53**, 11478–11482 (2014).
16. Montoya, J. H. et al. Materials for solar fuels and chemicals. *Nat. Mater.* **16**, 70–81 (2017).
17. Gust, D., Moore, T. A. & Moore, A. L. Solar fuels via artificial photosynthesis. *Acc. Chem. Res.* **42**, 1890–1898 (2009).
18. Li, P. F. et al. Large-scale nanophotonic solar selective absorbers for high-efficiency solar thermal energy conversion. *Adv. Mater.* **27**, 4585–4591 (2015).
19. Mandal, J. et al. Scalable, "dip-and-dry" fabrication of a wide-angle plasmonic selective absorber for high-efficiency solar-thermal energy conversion. *Adv. Mater.* **29**, 1702156 (2017).
20. Lu, J. L. et al. Coking- and sintering-resistant palladium catalysts achieved through atomic layer deposition. *Science* **335**, 1205–1208 (2012).
21. Jones, J. et al. Thermally stable single-atom platinum-on-ceria catalysts via atom trapping. *Science* **353**, 150–154 (2016).
22. Qi, Y. H. et al. Photoinduced defect engineering: Enhanced photothermal catalytic performance of 2D black In_2O_{3-x} nanosheets with bifunctional oxygen vacancies. *Adv. Mater.* **32**, 1903915 (2020).
23. Cai, M. J. et al. Greenhouse-inspired supra-photothermal CO_2 catalysis. *Nat. Energy* **6**, 807–814 (2021).
24. Wu, Z. Y. et al. Mo_2TiC_2 MXene-supported Ru clusters for efficient photothermal reverse water-gas shift. *ACS Nano* **17**, 1550–1559 (2023).
25. Wu, Z. Y. et al. Niobium and titanium carbides (MXenes) as superior photothermal supports for CO_2 photocatalysis. *ACS Nano* **15**, 5696–5705 (2021).
26. Li, Y. G. et al. General heterostructure strategy of photothermal materials for scalable solar-heating hydrogen production without the consumption of artificial energy. *Nat. Commun.* **13**, 776 (2022).
27. Li, Y. G. et al. Selective light absorber-assisted single nickel atom catalysts for ambient sunlight-driven CO_2 methanation. *Nat. Commun.* **10**, 2359 (2019).
28. Shahzad, F. et al. Electromagnetic interference shielding with 2D transition metal carbides (MXenes). *Science* **353**, 1137–1140 (2016).
29. Wang, J. F., Shen, M. M., Liu, Z. X. & Wang, W. J. MXene materials for advanced thermal management and thermal energy utilization. *Nano Energy* **97**, 107177 (2022).
30. Naguib, M. et al. Two-dimensional nanocrystals produced by exfoliation of Ti_3AlC_2. *Adv. Mater.* **23**, 4248–4253 (2011).
31. VahidMohammadi, A., Rosen, J. & Gogotsi, Y. The world of two-dimensional carbides and nitrides (MXenes). *Science* **372**, eabf1581 (2021).
32. Li, L. et al. Ultrathin titanium carbide (MXene) films for high-temperature thermal camouflage. *Adv. Funct. Mater.* **31**, 2101381 (2021).
33. Li, Y. et al. 2D $Ti_3C_2T_x$ MXenes: visible black but infrared white materials. *Adv. Mater.* **33**, 2103054 (2021).
34. Zhao, M. Q. et al. Hollow MXene spheres and 3D macroporous MXene frameworks for Na-ion storage. *Adv. Mater.* **29**, 1702410 (2017).
35. Abe, T., Tanizawa, M., Watanabe, K. & Taguchi, A. CO_2 methanation property of Ru nanoparticle-loaded TiO_2 prepared by a polygonal barrel-sputtering method. *Energy Environ. Sci.* **2**, 315–321 (2009).
36. Omi, S. et al. Synthesis of uniform PMMA microspheres employing modified SPG (shirasu porous glass) emulsification technique. *J. Appl. Polym. Sci.* **57**, 1013–1024 (1995).
37. Chen, Y. et al. Cooperative catalysis coupling photo-/photothermal effect to drive Sabatier reaction with unprecedented conversion and selectivity. *Joule* **5**, 3235–3251 (2021).
38. Ramalingam, V. et al. Heteroatom-mediated interactions between ruthenium single atoms and an MXene support for efficient hydrogen evolution. *Adv. Mater.* **31**, 1903841 (2019).
39. Zhou, L. et al. Self-assembly of highly efficient, broadband plasmonic absorbers for solar steam generation. *Sci. Adv.* **2**, e1501227 (2016).
40. Kelso, M. V., Mahenderkar, N. K., Chen, Q. Z., Tubbesing, J. Z. & Switzer, J. A. Spin coating epitaxial films. *Science* **364**, 166–169 (2019).
41. Anasori, B., Lukatskaya, M. R. & Gogotsi, Y. 2D metal carbides and nitrides (MXenes) for energy storage. *Nat. Rev. Mater.* **2**, 16098 (2017).
42. Dong, C. Y. et al. Size-dependent activity and selectivity of carbon dioxide photocatalytic reduction over platinum nanoparticles. *Nat. Commun.* **9**, 1252 (2018).
43. Deeva, E. B. et al. In situ XANES/XRD study of the structural stability of two-dimensional molybdenum carbide Mo_2CT_x: implications for the catalytic activity in the water–gas shift reaction. *Chem. Mater.* **31**, 4505–4513 (2019).
44. Zhou, H. et al. Engineering the Cu/Mo_2CT_x (MXene) interface to drive CO_2 hydrogenation to methanol. *Nat. Catal.* **4**, 860–871 (2021).
45. Zhao, H. B. et al. The role of Cu_1-O_3 species in single-atom Cu/ZrO_2 catalyst for CO_2 hydrogenation. *Nat. Catal.* **5**, 818–831 (2022).
46. Huynh, H. L. et al. Promoting effect of Fe on supported Ni catalysts in CO_2 methanation by in situ DRIFTS and DFT study. *J. Catal.* **392**, 266–277 (2020).
47. Zhou, J. et al. Interfacial compatibility critically controls Ru/TiO_2 metal-support interaction modes in CO_2 hydrogenation. *Nat. Commun.* **13**, 327 (2022).
48. Wu, C. Y. et al. Inverse ZrO_2/Cu as a highly efficient methanol synthesis catalyst from CO_2 hydrogenation. *Nat. Commun.* **11**, 5767 (2020).
49. Kattel, S., Liu, P. & Chen, J. G. Tuning selectivity of CO_2 hydrogenation reactions at the metal/oxide interface. *J. Am. Chem. Soc.* **139**, 9739–9754 (2017).
50. Wang, J. J. et al. A highly selective and stable ZnO-ZrO_2 solid solution catalyst for CO_2 hydrogenation to methanol. *Sci. Adv.* **3**, e1701290 (2017).
51. Kresse, G. & Hafner, J. Ab initio molecular dynamics for open-shell transition metals. *Phys. Rev. B* **48**, 13115–13118 (1993).
52. Kresse, G. & Furthmüller, J. Efficiency of ab-initio total energy calculations for metals and semiconductors using a plane-wave basis set. *Comput. Mater. Sci.* **6**, 15–50 (1996).
53. Kresse, G. & Furthmüller, J. Efficient iterative schemes for ab initio total-energy calculations using a plane-wave basis set. *Phys. Rev. B* **54**, 11169–11186 (1996).

54. Blöchl, P. E. Projector augmented-wave method. *Phys. Rev. B* **50**, 17953–17979 (1994).
55. Perdew, J. P., Burke, K. & Ernzerhof, M. Generalized gradient approximation made simple. *Phys. Rev. Lett.* **77**, 3865–3868 (1996).
56. Grimme, S. Semiempirical GGA-type density functional constructed with a long-range dispersion correction. *J. Comput. Chem.* **27**, 1787–1799 (2006).

Acknowledgements

We sincerely thank Kuibo Yin (Southeast University) for his kind help in measuring the transmission electron microscope. We acknowledge the micro-fabrication center at the National Laboratory of Solid State Microstructures (NLSSM) for technical support. J.Z. acknowledges support from the XPLORER PRIZE. This work is jointly supported by the National Key Research and Development Program of China (numbers 2022 YFA1404704, 2021YFA1400700 and 2020YFA0406104), National Natural Science Foundation of China (numbers 52372197, 51925204, 52002168, 12022403, 11874211, 61735008, 62134009 and 62121005), Natural Science Foundation of Jiangsu Province (BK20231540), Excellent Research Programme of Nanjing University (ZYJH005), research foundation of Frontiers Science Center for Critical Earth Material Cycling (14380214), State Key Laboratory of New Textile Materials and Advanced Processing Technologies (Wuhan Textile University, No. FZ2022011) and the Fundamental Research Funds for the Central Universities (numbers 021314380184, 021314380208, 021314380190, 021314380140 and 021314380150).

Author contributions

B.Z. and J.Z. conceived and designed the project. Z.W.Y. and Z.X.L. conceived and designed the experiments. Z.W.Y. performed the key experiments and analyzed the results. Z.W.Y. and Z.X.L. assisted to carry out the in-situ DRIFTS characterization. T.J.L. and W.L. assisted to carry out optical simulations. L.P.D. and F.D. assisted to perform DFT calculations. W.B.Z. and Y.Y. assisted to perform TEM characterization. Z.W.Y. and Z.H.L. assisted to carry out thermal-field simulations. Z.P.C., Y.J., J.L.L., S.Y.R., W.X.L., J.Y.F., X.Z., and Z.S.L. provided support in the details of the experiment. Z.W.Y., Z.-Y.W., Z.X.L., B.Z., and J.Z. co-wrote the manuscript. All the authors discussed the results and commented on the manuscript.

Competing interests

The authors declare no competing interests.

Additional information

Supplementary information The online version contains supplementary material available at https://doi.org/10.1038/s41467-024-51896-4.

Correspondence and requests for materials should be addressed to Bin Zhu or Jia Zhu.

Peer review information *Nature Communications* thanks the anonymous reviewers for their contribution to the peer review of this work. A peer review file is available.

[1]National Laboratory of Solid State Microstructures, College of Engineering and Applied Sciences, Jiangsu Key Laboratory of Artificial Functional Materials, Frontiers Science Center for Critical Earth Material Cycling, Collaborative Innovation Center of Advanced Microstructures, Nanjing University, Nanjing, PR China. [2]Department of Chemistry, Institute of Innovative Material, Guangdong Provincial Key Laboratory of Sustainable Biomimetic Materials and Green Energy, Southern University of Science and Technology, Shenzhen, Guangdong, PR China. [3]Department of Chemical and Biomolecular Engineering, Rice University, Houston, TX, USA. [4]GPL Photonics Laboratory, State Key Laboratory of Luminescence and Applications, Changchun Institute of Optics, Fine Mechanics and Physics, Chinese Academy of Sciences, Changchun, Jilin, PR China. [5]School of Electronic Information and Artificial Intelligence, Shaanxi University of Science & Technology, Xi'an, China. [6]Institute of Technology for Carbon Neutrality, Shenzhen Institute of Advanced Technology, Chinese Academy of Sciences, Shenzhen, China. [7]School of Physical Science and Technology, ShanghaiTech University, Shanghai, China. [8]These authors contributed equally: Zhengwei Yang, Zhen-Yu Wu, Zhexing Lin. ✉e-mail: binzhu@nju.edu.cn; jiazhu@nju.edu.cn